

Article

Preparation of Au@ZnO Nanofilms by Combining Magnetron Sputtering and Post-Annealing for Selective Detection of Isopropanol

Guodong Wang¹, Pengju Wu¹, Lanlan Guo^{1,*} , Wei Wang², Wenqiang Liu¹, Yuanyuan Wang¹, Tingyu Chen¹, Haohan Wang¹, Yonghao Xu¹ and Yingli Yang³

¹ School of Physics and Electronic Information Engineering, Henan Polytechnic University, Jiaozuo 454003, China; wgd@hpu.edu.cn (G.W.); wu10072805@163.com (P.W.); lwq18739106528@163.com (W.L.); wyywsn422@163.com (Y.W.); chen1465703951@163.com (T.C.); haohan0721@163.com (H.W.); yonghaoxu@hpu.edu.cn (Y.X.)

² State Key Laboratory on Integrated Optoelectronics, College of Electronic Science and Engineering, Jilin University, Changchun 130021, China; ww@jlu.edu.cn

³ Instrumental Analysis Center, Henan Polytechnic University, Jiaozuo 454003, China; yangyingli@hpu.edu.cn

* Correspondence: guolanlan@hpu.edu.cn

Abstract: We demonstrate the highly sensitive and fast response/recovery gas sensors for detecting isopropanol (IPA), in which the Au-nanoparticles-modified ZnO (Au@ZnO) nanofilms act as the active layers. The data confirm that both the response and the response/recovery speed for the detection of IPA are significantly improved by adding Au nanoparticles on the surface of ZnO nanofilms. The gas sensor with an Optimum Au@ZnO nanofilm exhibits the highest responses of 160 and 7 to the 100 and 1 ppm IPA at 300 °C, which indicates high sensitivity and a very low detecting limit. The sensor also exhibits a very short response/recovery time of 4/15 s on the optimized Au@ZnO nanofilm, which is much shorter than that of the sensor with a pure ZnO nanofilm. The mechanisms of the performance improvement in the sensors are discussed in detail. Both the electronic sensitization and the chemical sensitization of the ZnO nanofilms are improved by the modified Au nanoparticles, which not only regulate the thickness of the depletion layer but also increase the amount of adsorbed oxygen species on the surfaces. This work proposes a strategy to develop a highly sensitive gas sensor for real-time monitoring of IPA.

Keywords: ZnO nanofilm; IPA; Au nanoparticles; magnetron sputtering



Citation: Wang, G.; Wu, P.; Guo, L.; Wang, W.; Liu, W.; Wang, Y.; Chen, T.; Wang, H.; Xu, Y.; Yang, Y. Preparation of Au@ZnO Nanofilms by Combining Magnetron Sputtering and Post-Annealing for Selective Detection of Isopropanol. *Chemosensors* **2022**, *10*, 211. <https://doi.org/10.3390/chemosensors10060211>

Academic Editors: Bilge Saruhan-Brings, Roussin Lontio Fomekong and Svitlana Nahirniak

Received: 15 April 2022

Accepted: 31 May 2022

Published: 3 June 2022

Publisher's Note: MDPI stays neutral with regard to jurisdictional claims in published maps and institutional affiliations.



Copyright: © 2022 by the authors. Licensee MDPI, Basel, Switzerland. This article is an open access article distributed under the terms and conditions of the Creative Commons Attribution (CC BY) license (<https://creativecommons.org/licenses/by/4.0/>).

1. Introduction

IPA is widely used as a solvent and a synthetic chemical intermediate in industrial production, pharmaceutical electronics, agricultural industries and many other fields [1,2]. Long-term exposure to IPA gas will cause serious harm to human health and safety, in the nervous system, respiratory system and visual system [3,4]. In addition, detection of the IPA concentration in the exhaled gas can be used as one of the biomarkers for early diagnosis of lung cancer [5–7]. Therefore, it is very much desired to develop a highly sensitive and reliable gas sensor for detecting the IPA molecules. Many materials, such as metal oxide semiconductors (MOS), compound semiconductors, conductive polymers and composite metal oxides, have been used for gas detection [8–11]. Attributed to the advantages of high performance, low cost, small volume and easy operation, the MOS-based gas sensors are an effective device for detecting various toxic, flammable and explosive gases, including IPA [12–17].

So far, there are few reports about the IPA gas sensors with high sensitivity and fast response/recovery speed. For instance, porous Pt-functionalized SnO₂ sheets were prepared by a facile solution combustion synthesis and were used to build a gas sensor to

show a response value of 190.50 for 100 ppm IPA at the selected temperature of 220 °C [18]. Shanhong Li and Zhen Jin have reported a good gas sensor with the detecting limit on the IPA gas as low as 1 ppm, by preparing the SnO₂ nanorings with a facile hydrothermal method [19]. However, the response and recovery times are as long as 6.8 and 38.6 s, respectively, which is unfavorable for real-time monitoring of the IPA gas. Although the Fe-doped ZnO nanoneedles have been synthesized and used to effectively detect the IPA gas with a responsivity of 4.7 even at the low concentrations of 250 ppb IPA, the sensor shows a slow response and recovery speed, with the times up to 51 and 762 s, respectively [20]. In contrast, the BiFeO₃ nanocrystals-based sensors show a fast response and recovery speed with the times of 6 and 17 s to detect the IPA gas, respectively, but with a small response of only 31 at a concentration of 100 ppm [21].

It is an effective method to improve the sensitivity of gas sensors by adding the noble metals on the MOS gas sensors as the catalysts. For example, Cheng et al. changed the number of Au precursors by chemical deposition to control the coverage of Au nanoparticles on ZnO surface, so as to improve the gas sensing characteristics of the ZnO gas sensor [22]. Guo et al. fixed Au nanoparticles on ZnO nanorods by the reduction method. Compared with pure ZnO materials, the gas sensing performance of the ZnO gas sensor modified by Au nanoparticles was significantly improved [23]. The noble metals nanoparticles on the ZnO surface have a strong spillover effect, which can dissociate O₂ into the adsorbed oxygen species. The oxygen species will be spilled onto the surface of ZnO and thus improve the gas sensitivity [24–26]. However, the agglomeration of particles also exists in the deposition of noble metal by chemical methods.

Another noteworthy problem is that the reported gas sensors are normally fabricated by screen printing or dip coating onto a hot plate from the slurry-like precursors, which results in a large device-to-device variation, due to the non-uniform composition in the slurry or the non-uniform thickness of films [27]. However, in contrast, controllable and uniform thickness is easily obtained on the MOS nanofilms by magnetron sputtering, which is desirable for fabricating the gas sensors with good uniformity [28–31]. On the other hand, the magnetron-sputtered MOS nanofilms are dense; therefore, the corresponding gas sensors show poor sensitivity and require high operating temperature, which is a disadvantage for the practical application [32].

In this work, we deposit the Au-nanoparticles-modified ZnO (Au@ZnO) nanofilms by magnetron sputtering and sequential annealing, by which the gas sensors are fabricated to detect the IPA gas. Both the sensitivity and the response speed of the gas sensors are significantly improved by building the Au@ZnO nanofilms. The Au@ZnO nanofilms are optimized to improve the performances of sensors for detecting the IPA gas. In addition, the mechanisms of the improvement of the sensor performances are discussed in detail. As a result, the optimized gas sensors exhibit high sensitivity, good selectivity and fast response/recovery capability.

2. Experimental Section

The targets of ZnO and Au, with a purity of 99.99% and sizes of 60 and 5 mm in diameter and thickness, respectively, were used. Prior to deposition, the Si substrates, with an area of 1 cm × 1 cm as cut from Si wafers, were ultrasonically cleaned in acetone, absolute ethanol and deionized water in sequence for 15 min. The ZnO nanofilms with a thickness of 24 nm were deposited on the cleaned Si substrates by RF magnetron sputtering at a power of 50 W, argon flow of 40 sccm, sputtering pressure of 2.5 Pa and background pressure of 1.6×10^{-4} Pa. Subsequently, the Au ultrathin layers were deposited on the ZnO nanofilms by DC magnetron sputtering at a power of 20 W, argon flow of 40 sccm, sputtering pressure of 2.5 Pa and background pressure of 1.6×10^{-4} Pa. The sputtering times of the Au ultrathin layers were selected as 0 s, 5 s, 10 s and 20 s and the corresponding thickness of Au ultrathin layers was 0 nm, 0.5 nm, 1.3 nm and 2.2 nm, respectively. The corresponding samples were defined as S1, S2, S3 and S4, respectively. Next, the four samples were annealed at 600 °C for 2 hours in a tubular furnace, with a heating rate of

5 °C/min, in which the Au ultralayers were transformed into discrete Au nanoparticles. The preparation procedure of the nanofilms is shown in Figure 1.

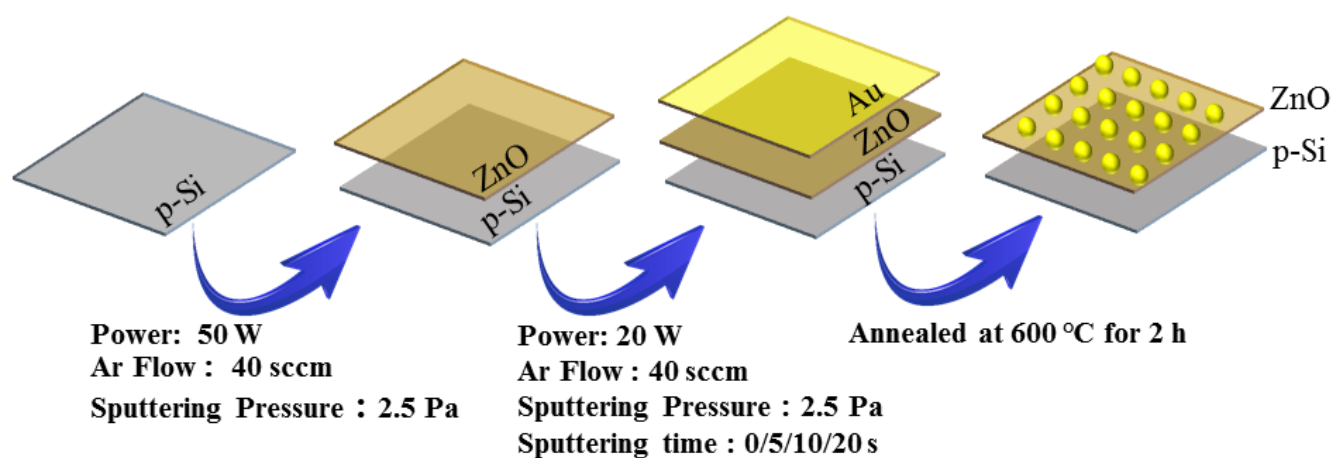


Figure 1. Schematic illustration for the preparation process of Au@ZnO nanofilms.

The surface morphologies of the films were observed by scanning electron microscopy (SEM, Merlin Compact, Carl Zeiss NTs GmbH, Oberkochen, Germany). The crystallinity, purity and composition were characterized by X-ray diffraction (XRD, Smartlab, Rigaku Corporation, Tokyo, Japan) with Cu-K α 1 radiation ($\lambda = 0.15406$ nm). The valence states of elements in the nanofilms were analyzed by using X-ray photoelectron spectroscopy (XPS, ESCALAB 250Xi, Thermo Scientific K-Alpha, Waltham, MA, USA).

The multifunctional gas sensing testing system (CGS-MT, Beijing Sino Aggtech, Beijing, China), which is composed of a temperature and humidity control system, a test chamber (5 L) with two sensor channels and a circulating water system, is used to analyze the gas sensing performance of the as-obtained samples. In each sensor channel, two metal probes of the CGS-MT were directly placed on the surface of ZnO films for resistance measurement. The data acquisition is achieved through test software on the computer connected to the CGS-MT instrument. The acquisition rate of the electrical resistance is once per second.

The sensing performance was studied under laboratory conditions (~30 RH%, 18 °C). The liquid of IPA and other gases to be tested was injected on the evaporation table (110 °C) in the test chamber through a micro syringe to evaporate rapidly, respectively. The gas was diffused rapidly in the test chamber through a fan. The corresponding gas concentration (e.g., IPA) can be derived from the following equation:

$$C = \frac{22.4 \times \varphi \times \rho \times V_1}{M \times V_2} \times 1000 \quad (1)$$

where C (ppm) and M (g/mol) are the concentration and the molecular weight of formaldehyde, respectively. φ and ρ (g/mL) represent the volume fraction (99.7%) and the density (0.784 g/mL) of the IPA aqueous solution, respectively. V_1 (μ L) and V_2 (5 L) are the volume of IPA aqueous solution to be injected and the volume of the test chamber, respectively.

The details of the complete test procedure are as follows. First, one must open the circulating water system and put the fabricated sensors into an air-filled test chamber for aging for three days. Afterwards, the sensor resistances gradually tend to reach a stable value, usually represented by R_a . Second, one must inject a certain concentration of target gas into the closed chamber with a micro-liter syringe. After a while, the resistance stabilizes again and is abbreviated as R_g . Then, one must open the lid of the chamber to refill the entire chamber with fresh air, and the resistance returns to near R_a again.

The sensitivity and response/recovery times are defined as follows. Taking n-type MOS sensor to detect reducing gas as an example, the sensitivity (S) is defined as R_a/R_g .

The response (τ_{res}) and recovery (τ_{recov}) times refer to the time periods from R_a changing to $R_a - |R_a - R_g| \times 90\%$ and from R_g changing to $R_g + |R_a - R_g| \times 90\%$, respectively.

3. Results and Discussion

3.1. Structural and Morphological Characteristics

Figure 2a shows the XRD spectra of the as-prepared Au@ZnO nanofilms. A sharp diffraction peak at 34.4° is observed on the four samples, which is assigned to the (002) orientation of hexagonal structure of ZnO (PDF#70-2551), indicating a highly preferred orientation of *c*-axis in the deposited ZnO nanofilms. Furthermore, a clear diffraction peak at 38.3° appeared on the XRD patterns of S2, S3 and S4, but not on S1, which is assigned to the (111) orientation of Au (PDF# 90-0056). No peaks from any other intermediates or crystalline phases are detected, which confirms the high purity of the as-prepared samples.

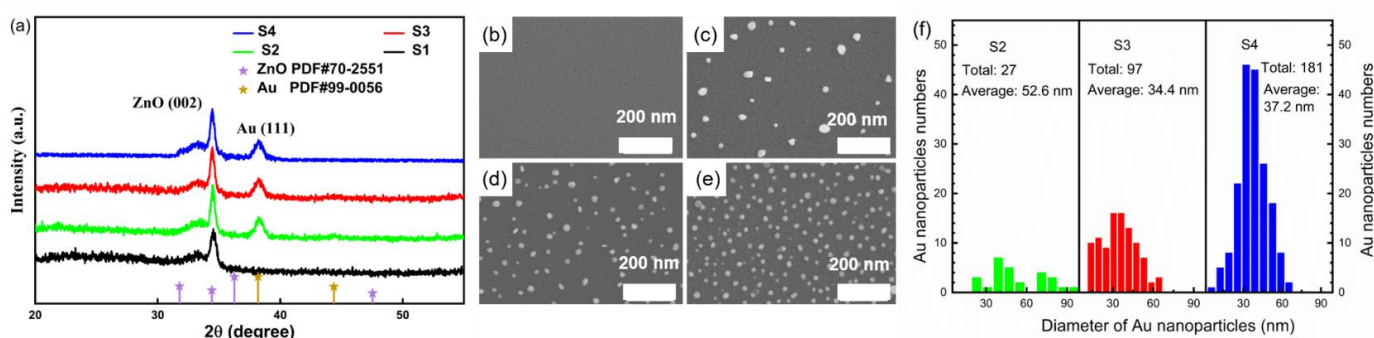


Figure 2. XRD patterns of as-obtained samples (a) and high-resolution SEM images of S1 (b); S2 (c); S3 (d); S4 (e); size distribution of Au nanoparticles (f).

Figure 2b–e show the high-resolution SEM images of the as-prepared Au@ZnO nanofilms. The pure ZnO nanofilm exhibits a clear smooth surface morphology, as shown in Figure 2b. While the clear and discrete nanoparticles with diameters of 20–100 nm are observed on the surface of S2 (Figure 2c), which are confirmed as Au nanoparticles, by combining the XRD pattern on Figure 2a. The Au nanoparticles are further confirmed by the results that the density of nanoparticles increases with the increasing deposition time of Au ultrathin layers (Figure 2d,e). For the three samples of S2, S3 and S4, the Au nanoparticles uniformly distribute on the surfaces of the ZnO nanofilms. Furthermore, the size distributions and quantity of Au nanoparticles in Figure 2c–e are shown in Figure 2f. The density of Au nanoparticles in S2, S3 and S4 is $9.18/\mu\text{m}^2$, $33/\mu\text{m}^2$ and $61.56/\mu\text{m}^2$, respectively. It can be seen that the density of Au nanoparticles increases with the increase of sputtering time. The size distributions of Au nanoparticles become more uniform and the average size of Au nanoparticles also changes significantly with the increase of the amount of Au (the increasing deposition time of Au ultrathin layers). The density and average size of the Au nanoparticles have an important effect on the gas sensing performances of the sensors to the targeted IPA gas, as discussed in detail later.

The composition and the valence status of the pure ZnO and Au@ZnO nanofilms are analyzed by the measurement of XPS, as shown in Figure 3. The characteristic peaks of Zn and O are clearly observed on the four samples (Figure 3a). Although the characteristic peak for Au 4f is not obvious on the Au@ZnO nanofilms due to the low content of Au and the position of Au overlap with Zn 3p, it is present on samples of S2, S3 and S4, but not on S1. The Zn $2p_{3/2}$ and $2p_{1/2}$ are located at 1020.95 eV and 1044.03 eV, respectively, and the interval between Zn $2p_{3/2}$ and $2p_{1/2}$ peaks is approximately 23.3 eV, as shown in Figure 3b, which confirms that the Zn–O bonds dominate in the films [33]. Figure 3c shows the fitted peaks of Au 4f and Zn 3p by Gauss. The peaks of Zn $3p_{1/2}$ and Au $4f_{7/2}$ shift towards high binding energy, while the peaks of Zn $3p_{3/2}$ and Au $4f_{5/2}$ exhibit a negligible shift with the increase of the amount of Au. In addition, the binding energy (83.01 and 86.67 eV for Au $4f_{7/2}$ and Au $4f_{5/2}$, respectively) of Au in Au@ZnO nanofilms

is much lower than that of bulk metallic Au (84.0 and 87.6 eV for Au 4f_{7/2} and Au 4f_{5/2}, respectively). The mechanism is attributed to the metal-semiconductor contacts. Normally, the work function of Au (5.35 eV) is larger than that of ZnO (5.10 eV), thus electrons flow from ZnO to Au to obtain an equilibrium Fermi level [18,34]. The electron loss in ZnO enhances the force binding to electrons, and thus increases the binding energy. In addition, the electron increment on the Au reduces the binding energy of Au 4f [18]. The O 1s spectra are fitted into two peaks, well corresponding to the lattice oxygen (O_L) and adsorbed oxygen (O_C) on the surface, respectively, as shown in Figure 3d [35]. Generally, the increase of the adsorbed oxygen in ZnO favors the IPA gas response. Table 1 lists the percentage of different components in O 1s for the Au@ZnO nanofilms, which intuitively shows the effect of the density of the Au nanoparticles on the amount of adsorbed oxygen species. The increase of the amount of adsorbed oxygen species with the increasing density of the Au nanoparticles is attributed to the spillover effect of Au nanoparticles, which can help to dissociate more oxygen molecules and generate more oxygen vacancies.

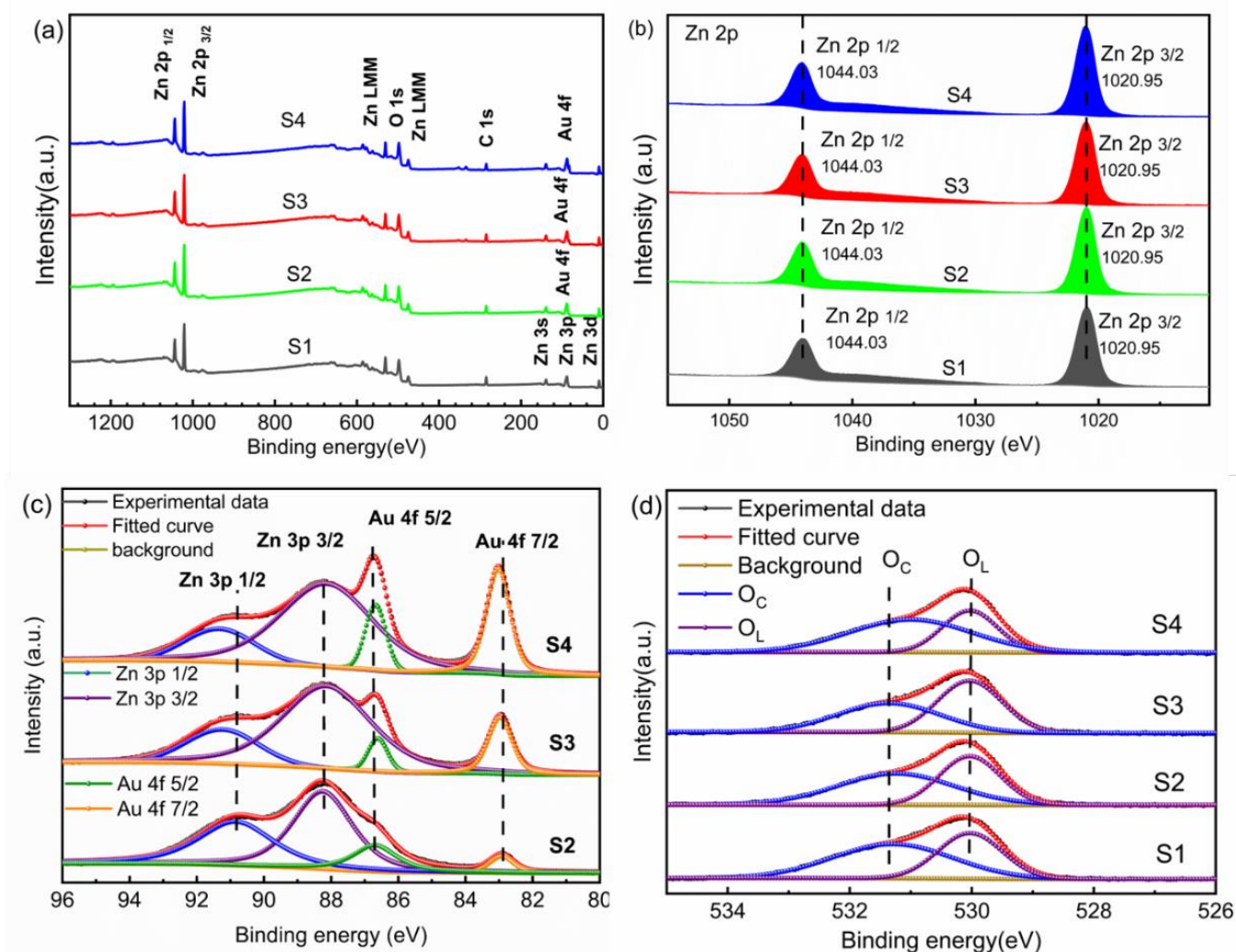


Figure 3. The XPS spectra of pure ZnO and Au@ZnO nanofilms; (a) survey; (b) Zn 2p; (c) Au 4f and Zn 3p; (d) O 1s.

Table 1. The percentage of different components in O 1s for Au@ZnO nanofilms.

Samples	Lattice Oxygen (O _L)	Adsorbed Oxygen (O _C)
S1	58.28%	41.72%
S2	56.11%	43.89%
S3	52.96%	47.04%
S4	45.20%	54.80%

3.2. Gas Sensing Properties to IPA

The response of the as-obtained samples toward 100 ppm IPA is tested at the operating temperature ranges of 225~375 °C. As is observed in Figure 4a, the initial resistance (R_a) of all as-obtained samples decreases with increasing temperature. This can be ascribed to the increase of electron-hole pairs with the increase of the temperature, leading to the decrease of resistance values. In addition, it is noteworthy that the initial resistance of the Au@ZnO nanofilms in the air is significantly larger than that of the pure ZnO nanofilms. Especially for S2, R_a increases by a factor of 49 greater than that of S1 (at 300 °C), as shown in Figure 4c. The increase of R_a is attributed to the metal-semiconductor contact, in which the formed Schottky barrier greatly decreases the conductivity of the films. While R_a of the Au@ZnO nanofilms in the air decreases with the further increasing density of Au nanoparticles, attributed to the easier charges transport in the greater Au nanoparticles and the smaller spacing between the Au nanoparticles. Figure 4b shows the dependence of the response of the sensors on the operating temperatures, which shows a volcano shape, especially for the sensors of S3 and S4, attributed to the mechanism of gas adsorption and desorption on ZnO nanofilms [36]. The best operating temperatures, at which the highest responses are obtained for each sensor, decrease with the increasing density of Au nanoparticles on the ZnO nanofilms. Specifically, the best operating temperatures are 350, 325, 300 and 300 °C for the sensors of S1, S2, S3 and S4, respectively. The results indicate that the catalysis of Au nanoparticles favors a decrease of the operating temperature of the ZnO-nanofilm-based sensors for detecting IPA. Furthermore, the Au nanoparticles have a significant contribution to the improvement of the sensitivity of the ZnO-nanofilm-based sensors to the IPA gas. The responses of the sensors, operating at the best temperature, significantly increase with the increasing density of the Au nanoparticles (the corresponding sputtering times of the Au ultrathin layers increasing to 10 s from 0 s), as shown in Figure 4d. These results confirm the catalysis of the Au nanoparticles on the detection of the ZnO nanofilms to IPA gas. Because the response of the sensors decreases with the further increase of the density of the Au nanoparticles (the corresponding sputtering times of the Au ultrathin layers increasing to 20 s from 10 s), S3 exhibited the highest response. The reason can be explained as follows. The improvement of gas sensing performances of the Au@ZnO nanofilms can be attributed to both the chemical sensitization and electronic sensitization. XPS results showed that S4 had the largest proportion of surface-adsorbed oxygen, which proved that the action of chemical sensitization reached the maximum. However, it can be seen that S2 possessed the biggest initial resistance from Figure 4c, which indicates that its electronic sensitization reached the maximum. Although the excessive modification of Au increased the proportion of surface-adsorbed oxygen, it also formed an independent electron transmission channel and reduced the electronic sensitization. In comparison, both the chemical sensitization and electronic sensitization of S3 are relatively strong. Under the joint action of chemical sensitization and electronic sensitization, the optimum gas sensitivity is achieved on the sensors of S3 with an optimum density of Au nanoparticles on the ZnO nanofilms.

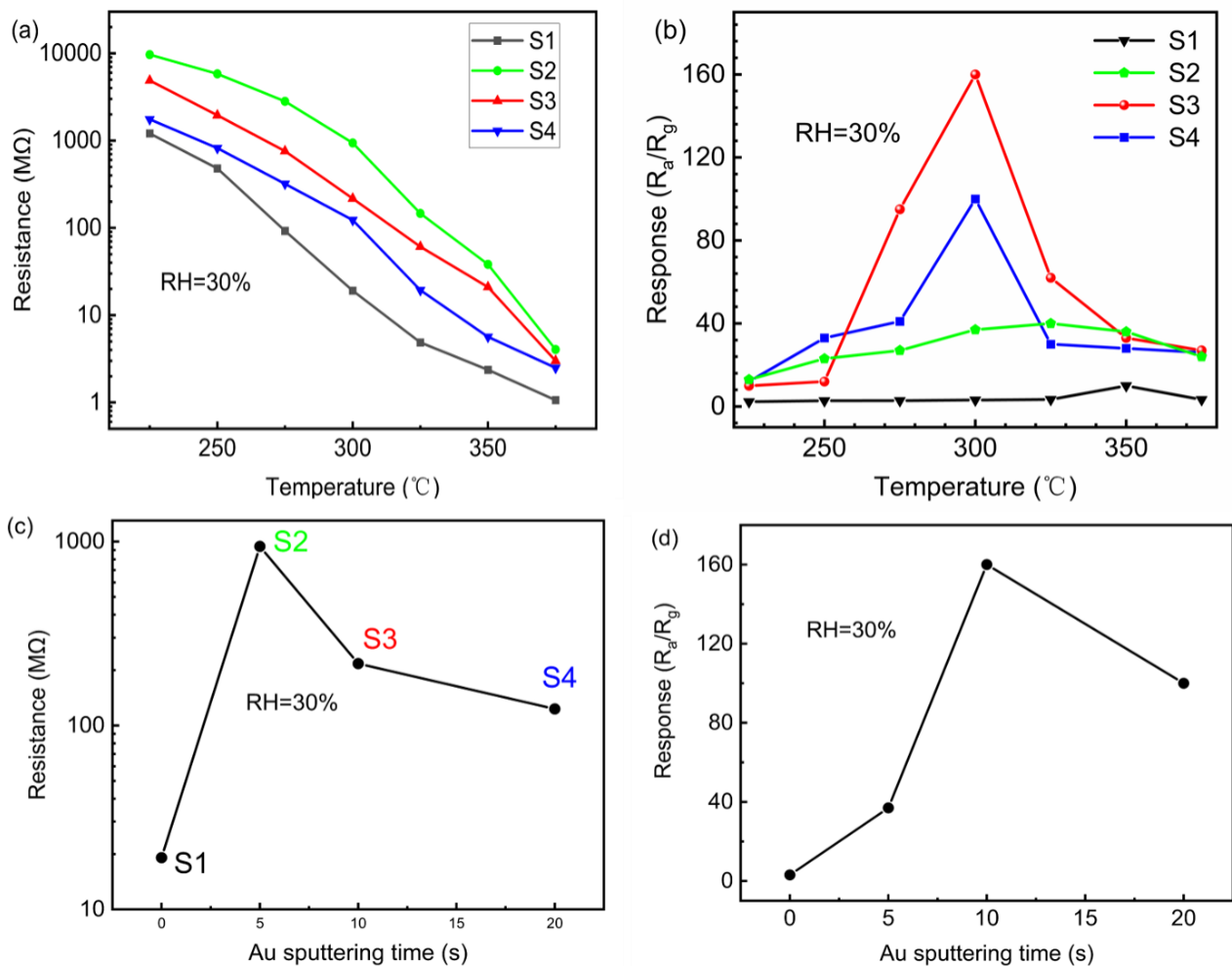


Figure 4. The initial resistance of as-obtained samples at various temperatures (a); the response of as-obtained samples toward 100 ppm IPA with operating temperatures (b); variation of initial resistance of all as-obtained samples at 300 $^{\circ}C$ with Au sputtering time (c); variation of response of all as-obtained samples toward 100 ppm IPA at 300 $^{\circ}C$ with Au sputtering time (d).

Figure 5 shows the dynamic response of the sensors to detect the 100 ppm IPA gas, at the optimum operating temperature of 300 $^{\circ}C$, in which the response times are extracted to be 6, 5, 4 and 2 for the sensors of S1, S2, S3 and S4, respectively. The recovery times are also extracted from the data on Figure 5, with the values of 56, 10, 15 and 14 for the sensors of S1, S2, S3 and S4, respectively. The results clearly demonstrate that the added Au nanoparticles on the ZnO nanofilms can accelerate the response/recovery process of the sensors to detect the IPA gas. This can be considered to be the spillover effect of Au nanoparticles, that is, the gas to be measured is adsorbed and activated on the Au nanoparticles, and then it flows to the oxide semiconductor, which promotes the surface reaction rate and shortens the response and recovery time.

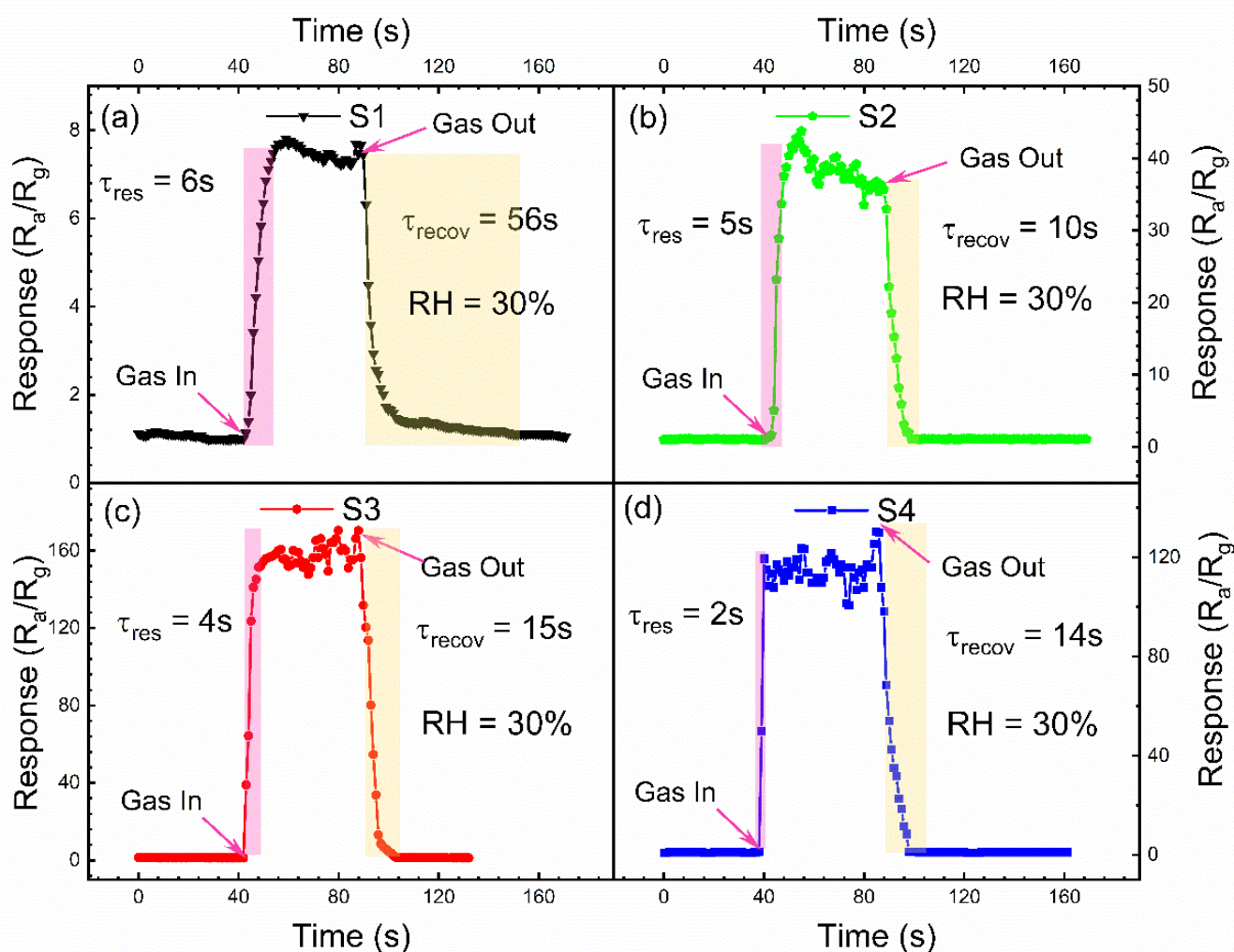


Figure 5. The dynamic response curves of as-obtained samples with time to 100 ppm IPA. (a) S1; (b) S2; (c) S3; (d) S4.

The selectivity, as an important figure of merit of the sensors, is also investigated on our Au@ZnO-nanofilms-based sensors. The sensitivity of the present sensors to the different gases of IPA, acetone ($C_3H_6O_3$), methanol (CH_3OH), ethanol (C_2H_5OH), xylene (C_8H_{10}), toluene (C_7H_8), benzene (C_6H_6) and ammonia (NH_3) is summarized in Figure 6a. Delightfully, the response of the four sensors to IPA is much higher than the response to the other interfering gases. Especially for the sensors of S3, it exhibits the highest response and the best selectivity. In addition, the long-term stability of the sensor is an indispensable factor for practical application, so the comparative studies on the S3 sample were conducted, as shown in Figure 6b. The measurements were performed every 3 days for 30 days. The results demonstrate that the proposed sensor presents a nearly constant response, indicating its distinctive long-term stabilities. We also noticed that in long-term stability measurement, the resistance in air of S3 changed greatly; it decreased by 17.4% at the maximum change. However, the change of resistance in air of S3 had little effect on its response. Since the static measurement process was adopted and the relative humidity and temperature remained unchanged during the test, we estimate that this change was caused by the different positions of metal probe on the film surface during each test.

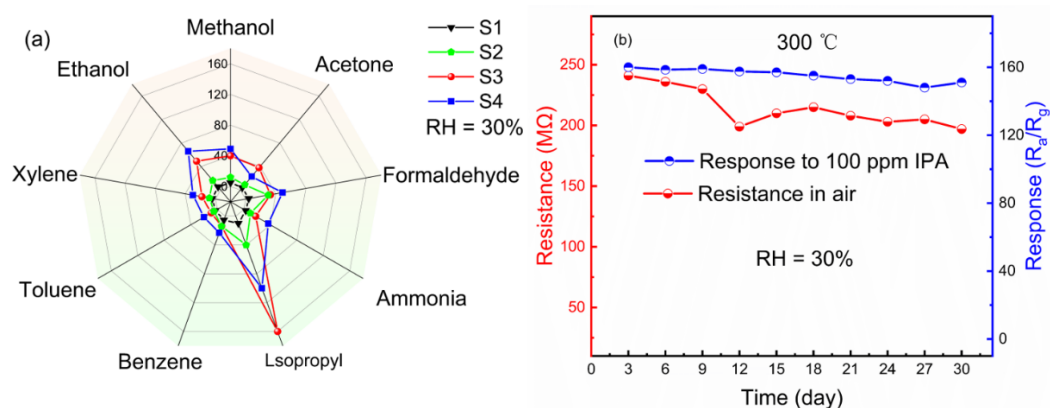


Figure 6. Selectivity of the four samples measured at 300 °C (a); long-term stability of S3 toward 100 ppm IPA at 300 °C (b).

The responses of the present four sensors to detect IPA at different concentrations in the range of 1~200 ppm are investigated, as shown in Figure 7. For all sensors, the responses increased with the increase of the IPA gas concentrations. The lower detection limit of sensor S1 is 30 ppm, as recorded in Figure 7a. The Au@ZnO-nanofilms-based sensors (S2, S3 and S4) not only exhibit higher responses but also show a better detection limit, which can effectively respond to the IPA gas even at the low concentration of 1 ppm (Figure 7b), compared with the pure ZnO-nanofilms-based sensors (S1). Among them, sensor S3 exhibited the highest response, with the responses up to 384 and 7 at the IPA gas concentrations of 200 and 1 ppm. For the four sensors, the dependence of the responses on the concentrations in the range of 1~200 ppm of the IPA gas to be detected is well-fitted as a linear function, which is favorable to the practical application, as shown in Figure 7c. The present Au@ZnO-nanofilms-based sensors exhibited outstanding advantages in the terms of response and detecting limit to detect the IPA gas, as compared with the other MOS sensors, as summarized in Table 2 [12–15,35]. The operating reliability of the Au@ZnO-nanofilms-based sensors was investigated by repeatedly recording the dynamic responses to the 100 ppm IPA gas at 300 °C, as shown in Figure 7d. It is most likely that the data of the responses to the IPA gas and the response/recovery times exhibit clear repeatability during the six exchanging cycles between the air and IPA gas, indicating high operational reliability in the present Au@ZnO-nanofilms-based sensors. Moreover, the responses of the Au@ZnO-nanofilms based-sensors quickly recover the initial values when the IPA gas is replaced by air for each cycle, indicating good reversibility. The excellent sensing performances of the Au@ZnO-nanofilms-based-sensors demonstrate that they are a promising candidate for the IPA detecting applications.

Table 2. Comparisons with the sensing properties of MOS-based IPA sensors reported in previous research.

Materials	Nano Structure	Concentration (ppm)	Temperature (°C)	Response (R_a/R_g)	Response/Recovery Time (s)	Limit of Detection (ppm)	Reference
Pt-SnO ₂	Porous sheet	100	220	190.5	/	5	[12]
SnO ₂	Nano rings	100	250	7.27	6.8/38.6	1	[13]
Fe-doped ZnO	Nano needles	5	275	23.6	51/762	0.25	[14]
BiFeO ₃	Nano crystal	100	240	31	6/17	2	[15]
ZnO-CdO	Porous	1000	248	174.8	16/25 (2000 ppm)	100	[24]
Au@ZnO	Nano film	100	300	160	4/15	1	This work

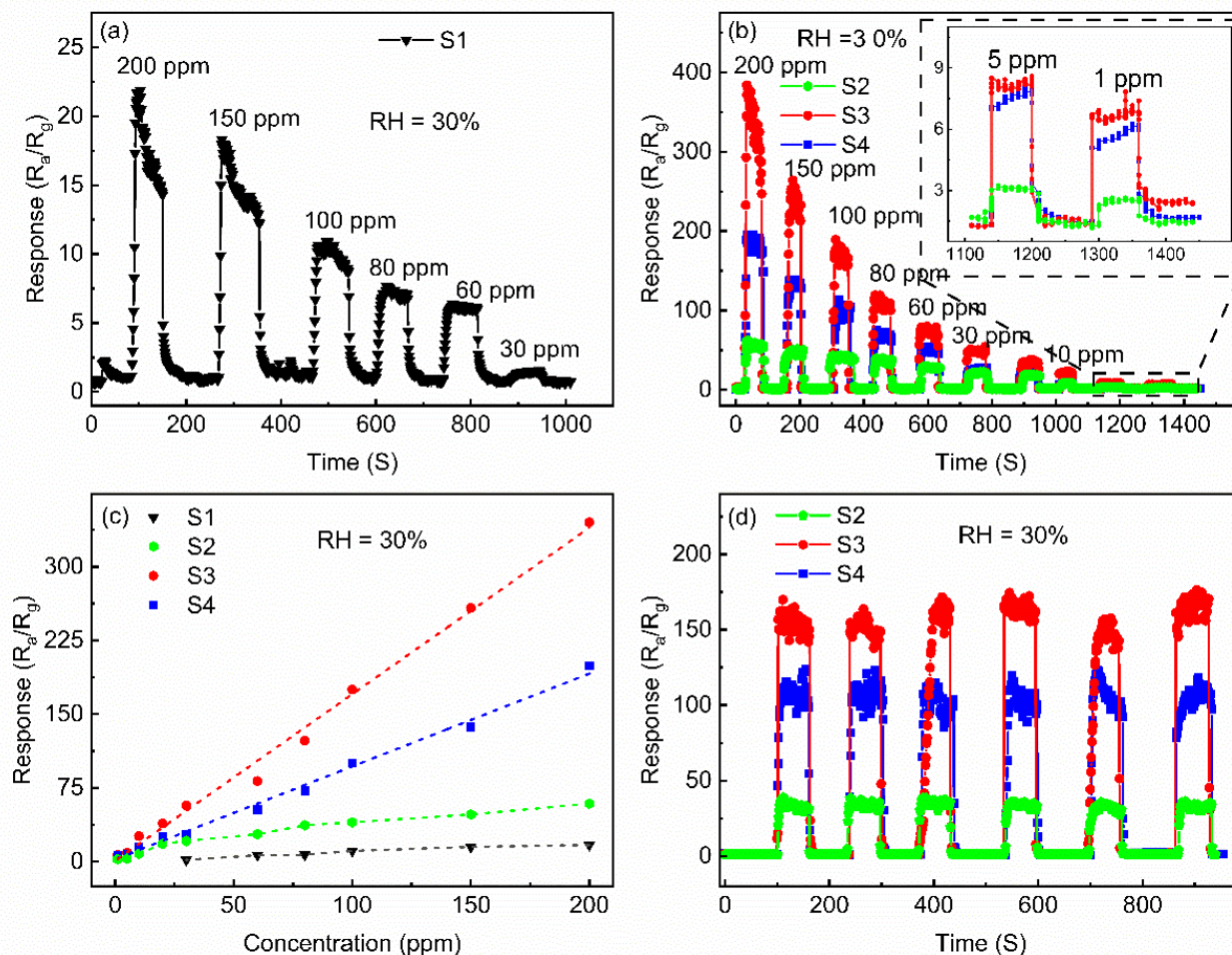


Figure 7. Transient response/recovery curves of pure ZnO nanofilm ranging from 30 to 200 ppm (a) and of Au@ZnO nanofilms ranging from 1 to 200 ppm (b); linearly fitting curve of response for the as-obtained samples (c); six periods of transient response/recovery curves of the Au@ZnO nanofilms to 100 ppm IPA at 300 °C (d).

3.3. Sensing Mechanism

Normally, ZnO is considered as an n-type metal oxide semiconductor, in which the majority carriers are electrons. The surface depletion layer dominates the conductivity of the ZnO nanofilms. The sensing mechanism of the ZnO nanofilm to the IPA gas is attributed to the change of the depletion layer thickness [17]. The formed metal-semiconductor contact by the Au nanoparticles on the ZnO nanofilms induces a Schottky barrier, which contributes to the enhancement of the sensing response in the sensors.

(i) In air, the oxygen molecules are adsorbed on the surfaces of the ZnO nanofilms, which obtain electrons from the conduction band of ZnO nanofilms and transform to negative oxygen ions (O_2^- , O^- and O^{2-}). The negative oxygen ions induce an electron depletion layer in the ZnO nanofilms adjacent to the surfaces, which increases the electrical resistance of sensors (Figure 8a). When the sensors are exposed to the IPA gas atmosphere, IPA molecules react with oxygen negative ions to produce H_2O and CO_2 molecules. The redox reaction equation is described as follows:



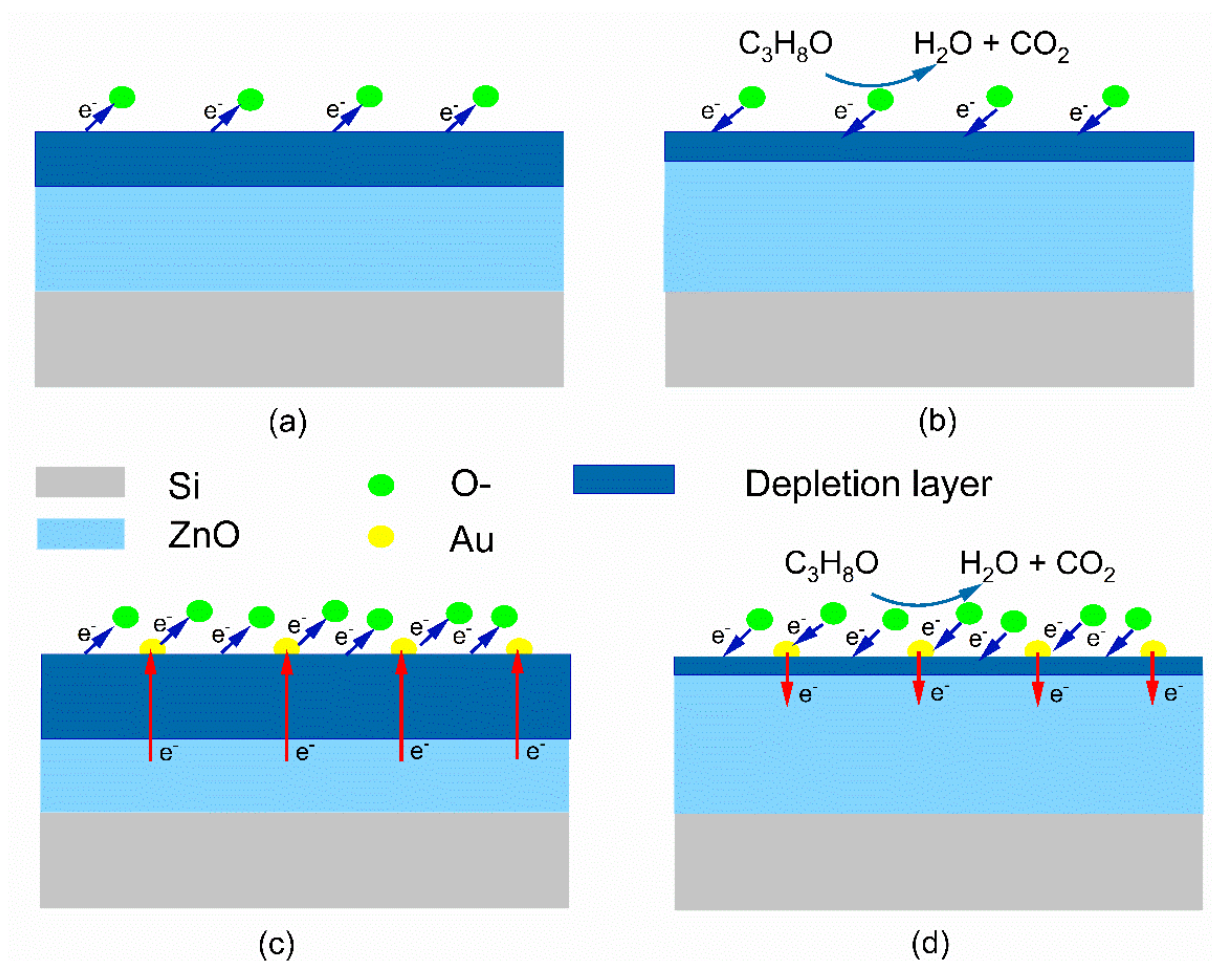


Figure 8. Schematic diagram of the sensing mechanism for pure ZnO nanofilm (a,b) and Au@ZnO nanofilms (c,d).

The electrons, produced by the redox reaction, return to the conduction band, which narrows down the depletion layer so that it is narrower, and reduces the resistance of ZnO nanofilms (Figure 8b).

(ii) The contacts of Au nanoparticles with ZnO nanofilms form the Schottky junctions. Many electrons transfer to the Au from the ZnO conduction band, which also produces an electron depletion layer in the ZnO nanofilms adjacent to the surfaces. The superposition of the electron depletion layers, induced by both the Au-ZnO contact and the O₂-ZnO contact, increases the initial resistance values of the Au@ZnO-nanofilms-based sensors in the air (Figure 8c). Furthermore, the Au nanoparticles also increase the adsorption of oxygen molecules on the Au@ZnO nanofilms, which is attributed to the spillover effect, by which more electrons are trapped and the electron depletion layer is further widened. When the Au@ZnO-nanofilms-based sensors are exposed to the IPA gas, many electrons produced by the redox reaction are returned to the conduction band, which narrows down the depletion layer (Figure 8d). In addition, Au nanoparticles play the role of catalyst, which accelerates the kinetics of the redox reactions on the surfaces and accelerates the response-recovery process of the sensors to detect the IPA gas.

(iii) The excellent gas sensing performances achieved on the Au@ZnO-nanofilms based-sensors are contributed by both the chemical sensitization and electronic sensitization. The increasing proportions of the surface-adsorbed oxygen on the Au@ZnO nanofilms indicate the increase of the chemical sensitization performance with the increase of the Au nanoparticles density, as demonstrated by the XPS measurements. Furthermore, the evolution of the initial resistance R_a on the four sensors with the increasing density of the

Au nanoparticles indicates the dependence of the electronic sensitization performance on the Au nanoparticles. The combination of the chemical sensitization and the electronic sensitization results in the best gas sensing performances being achieved on sensor S3, with an optimum density of Au nanoparticles on the ZnO nanofilms, which exhibit the highest response.

4. Conclusions

In summary, the Au@ZnO-nanofilms-based sensors are fabricated by magnetron sputtering and post-annealing. The measurements of XRD and SEM demonstrate the surface morphology characteristics of the processed Au@ZnO nanofilms, on which the Au nanoparticles uniformly distribute on the surface of ZnO nanofilms. The XPS measurement confirms the composition and the valence status of the Au@ZnO nanofilms. The density of the Au nanoparticles regulates the width of the electron depletion layer in the Au@ZnO nanofilms, and thus contributes the electronic sensitization of the sensors. Furthermore, the Au nanoparticles also increase the amount of adsorbed oxygen species on the surfaces of Au@ZnO nanofilms, and thus contribute the chemical sensitization of the sensors. The contributions from both the electronic sensitization and chemical sensitization of the Au@ZnO nanofilms significantly enhance the response and accelerate the response/recovery speed of the sensors to detect the IPA gas. The highest response of 160 to 100 ppm IPA and the very short response/recovery times of 4/15 s are achieved on the sensors S3 with an optimum density of Au nanoparticles on the Au@ZnO nanofilm, at the optimum operating temperature of 300 °C.

Author Contributions: G.W.: Conceptualization, Methodology, Data curation, Writing—original draft. P.W.: Methodology, Data curation, Investigation. L.G.: Conceptualization, Methodology, Writing—Review and editing. W.W.: Data curation. W.L.: Methodology. Y.W.: Investigation. T.C.: Data curation. H.W.: Data curation. Y.X.: Data curation. Y.Y.: Methodology. All authors have read and agreed to the published version of the manuscript.

Funding: This research was funded by the National Natural Science Foundation of China (62173128), the Innovative Scientists and Technicians Team of Henan Provincial High Education (21IRTSTHN016), the Fundamental Research Funds for the Universities of Henan Province (NSFRF210324) and the Doctoral Fund Project of Henan Polytechnic University (B2020-47).

Data Availability Statement: Not applicable.

Conflicts of Interest: The authors declare no conflict of interest.

References

1. Steinmann, D.; Faber, T.; Auwärter, V.; Heringhaus, C. Akute Intoxikation mit Isopropanol. *Der Anaesthetist* **2009**, *2*, 149–152. [[CrossRef](#)] [[PubMed](#)]
2. Verira, C.F.D.S.; Augusto, D.S.; Fancisco, M.F.; Rubens, M.F.; Adriano, P.M. Isopropanol-butanol-ethanol production by cell-immobilized vacuum fermentation. *Bioresour. Technol.* **2020**, *344*, 126313.
3. Lin, Y.T.; Huang, C.W.; Wang, Y.H.; Wu, J.C.S. High Effective composite RGO/TiO₂ photocatalysts to degrade isopropanol pollutant in semiconductor industry. *Top. Catal.* **2020**, *63*, 1240–1250. [[CrossRef](#)]
4. Slaughter, R.J.; Mason, R.W.; Beasley, D.M.G.; Vale, J.A.; Schep, L.J. Isopropanol poisoning. *Clin. Toxicol.* **2014**, *52*, 470–478. [[CrossRef](#)]
5. Zhang, Z.J.; Li, P.W.; Liu, L.P.; Ru, L.H.; Tang, H.X.; Feng, W.S. Amine-functionalized UiO-66 as a fluorescent sensor for highly selective detecting volatile organic compound biomarker of lung cancer. *J. Solid State Chem.* **2022**, *305*, 122623. [[CrossRef](#)]
6. Natale, C.D.; Paolesse, R.; Martinelli, E.; Capuano, R. Solid-state gas sensors for breath analysis: A review. *Anal. Chim. Acta* **2014**, *824*, 1–17. [[CrossRef](#)]
7. Salimi, M.; Hosseini, S.M.R.M. Smartphone-based detection of lung cancer-related volatile organic compounds (VOCs) using rapid synthesized ZnO nanosheet. *Sens. Actuators B Chem.* **2021**, *344*, 130127. [[CrossRef](#)]
8. Malik, R.; Tomer, V.K.; Mishra, Y.K.; Lin, L. Functional gas sensing nanomaterials: A panoramic view. *Appl. Phys. Rev.* **2020**, *7*, 021301. [[CrossRef](#)]
9. Zhou, T.; Zhang, T. Recent progress of nanostructured sensing materials from 0D to 3D: Overview of structure–property–application relationship for gas sensors. *Small Methods* **2021**, *5*, 2100215. [[CrossRef](#)]

10. Wu, J.; Yang, Y.L.; Liu, Z.G.; Wang, G.D. Strong sulfur passivation effects on the gas sensitivity of an $\text{In}_{0.3}\text{Ga}_{0.7}\text{As}$ surface quantum dots coupling structure. *J. Cryst. Growth* **2021**, *560–561*, 126058. [[CrossRef](#)]
11. Guo, L.; Zhang, B.; Yang, X.; Zhang, S.; Wang, Y.; Wang, G.; Zhang, Z. Sensing platform of $\text{PdO-ZnO-In}_2\text{O}_3$ nanofibers using MOF templated catalysts for triethylamine detection. *Sens. Actuators B Chem.* **2021**, *343*, 130126. [[CrossRef](#)]
12. Liu, X.H.; Wang, H.; Li, X.; Liu, D.; Wan, J.; Lai, X.; Hao, S.; Zhang, Q.; Chen, X. Fern-like metal-organic frameworks derived $\text{In}_2\text{O}_3/\text{ZnO}$ nanocomposite for superior triethylamine sensing properties. *Sens. Actuators B Chem.* **2021**, *345*, 130424. [[CrossRef](#)]
13. Jiao, M.; Chien, N.V.; Duy, N.V.; Hoa, N.D.; Hieu, N.V.; Hjort, K.; Nguyen, H. On-chip hydrothermal growth of ZnO nanorods at low temperature for highly selective NO_2 gas sensor. *Mater. Lett.* **2016**, *169*, 231–235. [[CrossRef](#)]
14. Wang, H.; Li, Y.; Wang, C.; Li, Y.; Bai, J.; Liu, Y.; Zhou, L.; Liu, F.; Shimanoe, K.; Lu, G. N-pentanol sensor based on ZnO nanorods functionalized with Au catalysts. *Sens. Actuators B Chem.* **2021**, *339*, 129888. [[CrossRef](#)]
15. Hung, P.S.; Chou, Y.S.; Huang, B.H.; Cheng, I.K.; Wang, G.R.; Chung, W.A.; Pan, F.M.; Wu, P.W. A vertically integrated ZnO-based hydrogen sensor with hierarchical bi-layered inverse opals. *Sens. Actuators B Chem.* **2020**, *325*, 128779. [[CrossRef](#)]
16. Pineau, N.J.; Krumeich, F.; Güntner, A.T.; Pratsinis, S.E. Y-doped ZnO films for acetic acid sensing down to ppb at high humidity. *Sens. Actuators B Chem.* **2021**, *327*, 128843. [[CrossRef](#)]
17. Guo, L.; Wang, Y.; Shang, Y.; Yang, X.; Zhang, S.; Wang, G.; Wang, Y.; Zhang, B.; Zhang, Z. Preparation of Pd/PdO@ZnO-ZnO nanorods by using metal organic framework templated catalysts for selective detection of triethylamine. *Sens. Actuators B Chem.* **2022**, *350*, 130804. [[CrossRef](#)]
18. Dong, C.; Liu, X.; Xiao, X.; Chen, G.; Wang, Y.; Djerdj, I. Combustion synthesis of porous Pt-functionalized SnO_2 sheets for isopropanol gas detection with a significant enhancement in response. *J. Mater. Chem. A* **2014**, *2*, 20089–20095. [[CrossRef](#)]
19. Li, S.H.; Chu, Z.; Meng, F.F.; Luo, T.; Hu, X.Y.; Huang, S.Z.; Jin, Z. Highly sensitive gas sensor based on SnO_2 nanorings for detection of isopropanol. *J. Alloy. Compd.* **2016**, *688*, 712–717. [[CrossRef](#)]
20. Luo, Y.; Ly, A.; Lahem, D.; Zhang, C.; Debliquy, M. A novel low-concentration isopropanol gas sensor based on Fe-doped ZnO nanoneedles and its gas sensing mechanism. *J. Mater. Sci.* **2021**, *56*, 3230–3245. [[CrossRef](#)]
21. Xu, H.X.; Xu, J.H.; Wei, J.L.; Zhang, Y. Fast response isopropanol sensing properties with sintered BiFeO_3 nanocrystals. *Materials* **2020**, *13*, 3829. [[CrossRef](#)] [[PubMed](#)]
22. Peng, C.; Liu, Y. Enhanced acetone sensing characteristics by decorating Au nanoparticles on ZnO flower-like structures. *Apply Phys. A-Mater. Sci. Processing* **2013**, *111*, 1151–1157. [[CrossRef](#)]
23. Guo, J.; Zhang, J.; Zhu, M.; Ju, D.; Xu, H.; Cao, B. High-performance gas sensor based on ZnO nanowires functionalized by Au nanoparticles. *Sens. Actuators B Chem.* **2014**, *199*, 339–345. [[CrossRef](#)]
24. Xu, Y.; Ma, T.; Zheng, L.; Sun, L.; Liu, X.; Zhao, Y.; Zhang, J. Rational design of $\text{Au/Co}_3\text{O}_4$ -functionalized $\text{W}_{18}\text{O}_{49}$ hollow heterostructures with high sensitivity and ultralow limit for triethylamine detection. *Sens. Actuators B Chem.* **2019**, *284*, 202–212. [[CrossRef](#)]
25. Zhou, X.; Xu, L.; Yang, S.; Zhu, S.; Chen, X.; Dong, B.; Bai, X.; Xu, W.; Lu, G.; Song, H. Highly dispersed Metal-Organic-Framework-Derived Pt nanoparticles on three-dimensional microporous ZnO for trace-level H_2S sensing. *Sens. Actuators B Chem.* **2020**, *309*, 127802. [[CrossRef](#)]
26. Zhang, X.; Liu, Y.; Liu, H.; Liang, T.; Zhang, P.; Dai, Z. $\text{FeSe}_2/\text{Hematite}$ n-n heterojunction with oxygen spillover for highly efficient NO_2 gas sensing. *Sens. Actuators B Chem.* **2021**, *345*, 130357. [[CrossRef](#)]
27. Wang, Y.; Liu, C.; Wang, Z.; Song, Z.; Zhou, X.; Han, N.; Chen, Y. Sputtered $\text{SnO}_2:\text{NiO}$ thin films on self-assembled Au nanoparticle arrays for MEMS compatible NO_2 gas sensors. *Sens. Actuators B Chem.* **2019**, *278*, 28–38. [[CrossRef](#)]
28. Chen, J.; Yan, X.; Liu, W.; Xue, Q. The ethanol sensing property of magnetron sputtered ZnO thin films modified by Ag ion implantation. *Sens. Actuators B Chem.* **2011**, *160*, 1499–1503. [[CrossRef](#)]
29. Al-Hardan, N.H.; Abdullah, M.J.; Aziz, A.A. Sensing mechanism of hydrogen gas sensor based on RF-sputtered ZnO thin films. *Int. J. Hydrog. Energy* **2010**, *35*, 4428–4434. [[CrossRef](#)]
30. Bhati, V.S.; Ranwa, S.; Fanetti, M.; Valant, M.; Kumar, M. Efficient hydrogen sensor based on Ni-doped ZnO nanostructures by RF sputtering. *Sens. Actuators B Chem.* **2018**, *255*, 588–597. [[CrossRef](#)]
31. Al-Hardan, N.; Abdullah, M.J.; Aziz, A.A. The gas response enhancement from ZnO film for H_2 gas detection. *Appl. Surf. Sci.* **2009**, *225*, 7794–7797. [[CrossRef](#)]
32. Teimoori, F.; Khojier, K.; Dehnavi, N.Z. Investigation on the electrical and methane gas-sensing properties of ZnO thin films produced by different methods. *J. Electron. Mater.* **2016**, *45*, 4881–4889. [[CrossRef](#)]
33. Xue, X.T.; Zhu, L.Y.; Yuan, K.P.; Zeng, C.; Li, X.X.; Ma, H.P.; Lu, H.L.; Zhang, D.W. ZnO branched p-Cu_xO @n-ZnO heterojunction nanowires for improving acetone gas sensing performance. *Sens. Actuators B Chem.* **2020**, *324*, 128729. [[CrossRef](#)]
34. Zheng, X.; Zhuo, Z.; Meng, S.; Wang, Y.; Li, D. Regulating charge transfer over 3D Au/ZnO hybrid inverse opal toward efficiently photocatalytic degradation of bisphenol A and photoelectrochemical water splitting. *Chem. Eng. J.* **2020**, *393*, 124676. [[CrossRef](#)]
35. Cai, X.; Hu, D.; Deng, S.; Han, B.; Wang, Y.; Wu, J.; Wang, Y. Isopropanol sensing properties of coral-like ZnO-CdO composites by flash preparation via self-sustained decomposition of metal-organic complexes. *Sens. Actuators B Chem.* **2014**, *198*, 402–410. [[CrossRef](#)]
36. Bai, H.; Guo, H.; Tan, Y.; Wang, J.; Dong, Y.; Liu, B.; Xie, Z.; Guo, F.; Chen, D.; Zhang, R.; et al. Facile synthesis of mesoporous CdS/PbS/SnO_2 composites for high-selectivity H_2 gas sensor. *Sens. Actuators B Chem.* **2021**, *340*, 129924. [[CrossRef](#)]